Supplement of Atmos. Chem. Phys., 24, 10639–10653, 2024
https://doi.org/10.5194/acp-24-10639-2024-supplement

Atmospheric Chemistry and Physics
Open Access
EGU

Supplement of

Quantifying large methane emissions from the Nord Stream pipeline gas leak of September 2022 using IASI satellite observations and inverse modelling

Chris Wilson et al.

Correspondence to: Chris Wilson (c.wilson@leeds.ac.uk)

Inverse modelling – analytical solution

Our inverse modelling method, like most, uses Bayesian theory in order to adapt the surface fluxes of CH_4 used in the TOMCAT model to produce the optimised model – observation comparison. These methods usually assume that the model variables to be optimised, contained within a state vector $\boldsymbol{x}$, have associated uncertainties of Gaussian distribution. This assumption allows the model – observation mismatch to be described via a cost function $J(\boldsymbol{x})$ as follows:

$$J(\boldsymbol{x}) = \frac{1}{2}(\boldsymbol{x} - \boldsymbol{x}_b)\boldsymbol{B}^{-1}(\boldsymbol{x} - \boldsymbol{x}_b) + \frac{1}{2}(\boldsymbol{y} - \boldsymbol{H}\boldsymbol{x})\boldsymbol{R}^{-1}(\boldsymbol{y} - \boldsymbol{H}\boldsymbol{x}) \quad (1)$$

Here, the vector $\boldsymbol{y}$ contains the observations, whilst the matrix $\boldsymbol{H}$ represents both the model transport and chemistry acting on the variables within the state vector, and the action of mapping the model output onto the observation space. The observation error covariance matrix $\boldsymbol{R}$ contains on its diagonal the uncertainties associated with the observations, model and model's representation of the observations. The off-diagonals contain the covariances between these uncertainties. Since these problems are generally under-constrained but the observational data, we also include an *a priori* estimate of the state vector, $\boldsymbol{x}_b$, and its own associated error covariance matrix $\boldsymbol{B}$. Minimising this cost function provides a solution that provides the best possible match between the model and the observations whilst remaining as close as possible to the *a priori* assumptions for the variables in the state vector.

There are various methods available to solve this minimisation problem, which can be difficult to achieve for larger problems with large matrices to invert. For such instances, TOMCAT has an iterative variational scheme, INVICAT, available (Wilson et al., 2014). However, the Nord Stream optimisation problem documented here is small enough that Equation *(1)* can be solved directly with basic computing software. The *a posteriori* solution for the state vector $\boldsymbol{x}_a$as documented by Tarantola and Valette (1982) can be solved for by assuming that the gradient of $J(\boldsymbol{x})$ is zero, as follows:

$$\boldsymbol{x}_a = \boldsymbol{x}_b + [\boldsymbol{H}^T\boldsymbol{R}^{-1}\boldsymbol{H} + \boldsymbol{B}^{-1}]^{-1}\boldsymbol{H}^T\boldsymbol{R}^{-1}(\boldsymbol{y} - \boldsymbol{H}\boldsymbol{x}_b) \quad (2)$$

whilst the *a posteriori* error covariance matrix $\boldsymbol{A}$ is given by:

$$\boldsymbol{A} = [\boldsymbol{H}^T\boldsymbol{R}^{-1}\boldsymbol{H} + \boldsymbol{B}^{-1}]^{-1}$$

We use separate 'tagged' tracers in the model to represent the atmospheric transport and chemistry for the members of $\boldsymbol{x}$, with each tracer sampled at the time and location of all satellite or *in situ* observations. These 'sensitivities' between the simulated mixing ratios and the state vector members fill the transport matrix $\boldsymbol{H}$. In our case, the state vector contains the Nord Stream leak emissions for each three-hour window, along with a separate tracer for the background CH_4 mixing ratios. All other information is contained in the main text in Section 3. TOMCAT has previously been used along with this method for the optimisation of emissions of CH_4 (McNorton et al., 2018) and halogenated very short lived substances (VSLS, Claxton et al. (2020)).

References

Claxton, T., Hossaini, R., Wilson, C., Montzka, S. A., Chipperfield, M. P., Wild, O., Bednarz, E. M., Carpenter, L. J., Andrews, S. J., Hackenberg, S. C., Mühle, J., Oram, D., Park, S., Park, M.-K., Atlas, E., Navarro, M., Schauffler, S., Sherry, D., Vollmer, M., Schuck, T., Engel, A., Krummel, P. B., Maione, M., Arduini, J., Saito, T., Yokouchi, Y., O'Doherty, S., Young, D., and Lunder, C.: A Synthesis Inversion to Constrain Global Emissions of Two Very Short Lived Chlorocarbons: Dichloromethane, and Perchloroethylene, Journal of Geophysical Research: Atmospheres, 125, e2019JD031818, https://doi.org/10.1029/2019JD031818, 2020.

McNorton, J., Wilson, C., Gloor, M., Parker, R. J., Boesch, H., Feng, W., Hossaini, R., and Chipperfield, M. P.: Attribution of recent increases in atmospheric methane through 3-D inverse modelling, Atmospheric Chemistry and Physics, 18, 18149–18168, https://doi.org/10.5194/acp-18-18149-2018, 2018.

Tarantola, A. and Valette, B.: Generalized nonlinear inverse problems solved using the least squares criterion, Reviews of Geophysics, 20, 219–232, https://doi.org/10.1029/RG020i002p00219, 1982.

Wilson, C., Chipperfield, M. P., Gloor, M., and Chevallier, F.: Development of a variational flux inversion system (INVICAT v1.0) using the TOMCAT chemical transport model, Geoscientific Model Development, 7, 2485–2500, https://doi.org/10.5194/gmd-7-2485-2014, 2014.

Supplementary Figures

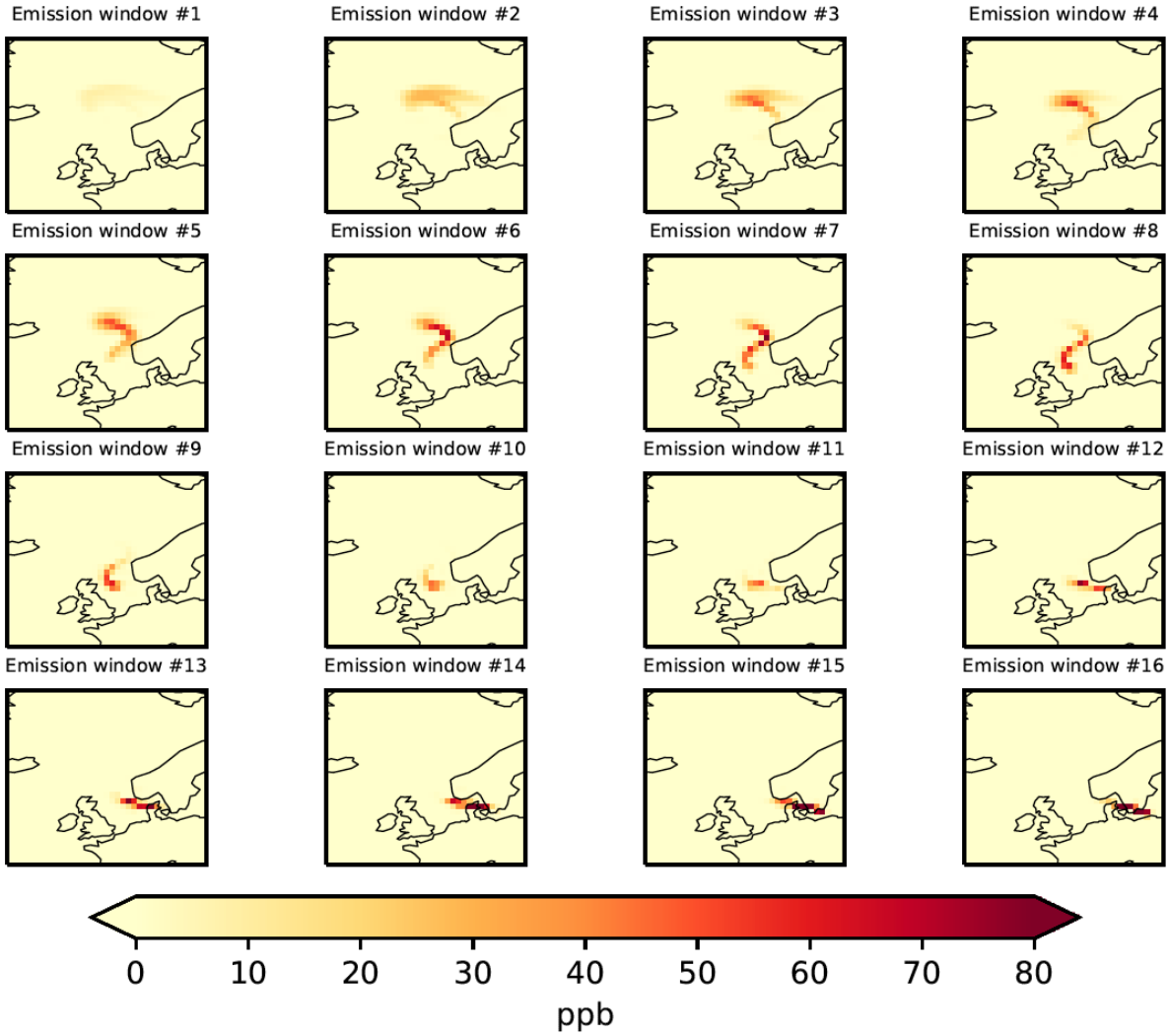

Figure S1: Simulated surface layer CH_4 [ppb] at 9.30am local time on 28th September 2022, for individual 3-hour emission widows over first two days of Nord Stream leaks. Flux from leaks is constant at 4.17 Gg hour^{-1}. Emission window #1 shows the transport of emissions from the first three hours of 26th September 2022, and subsequent panels correspond to subsequent 3-hour time emission windows.

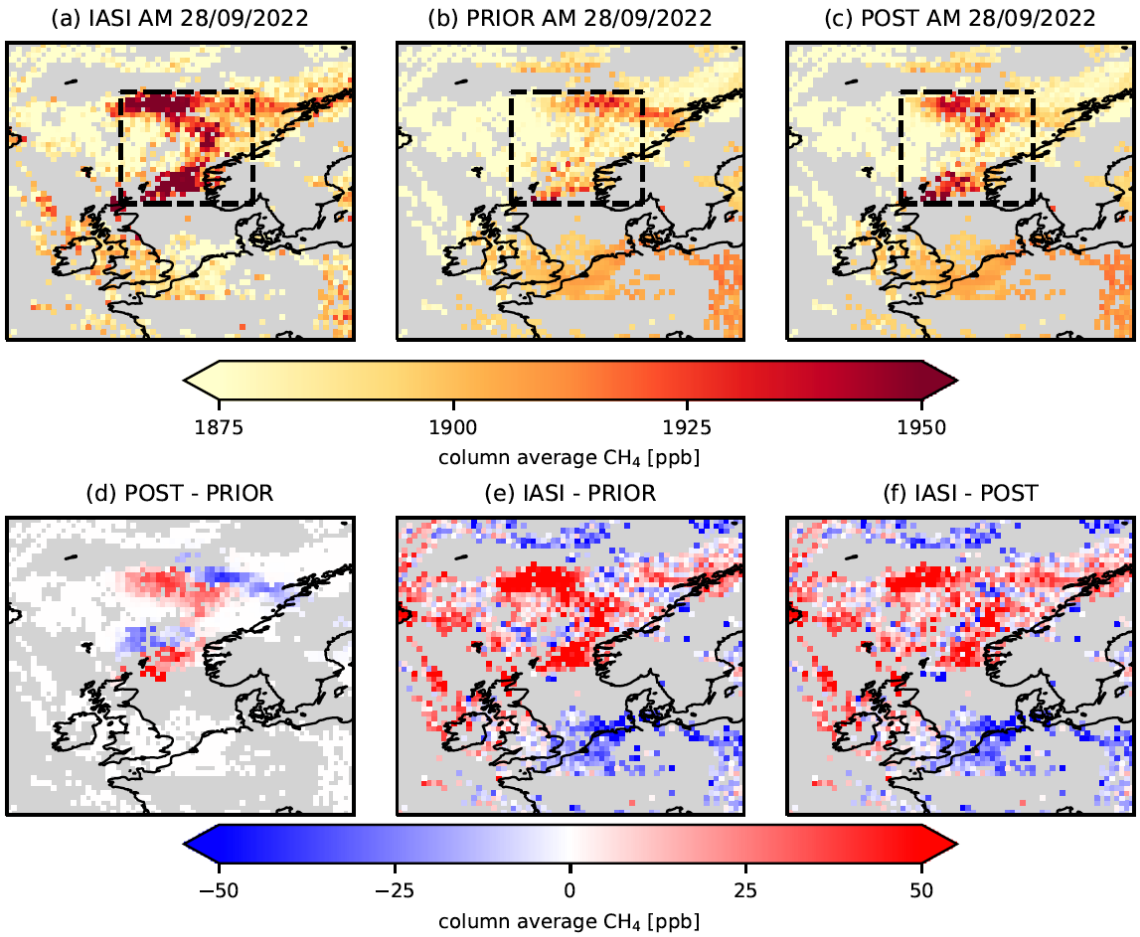

Figure S2: Column average CH_4 (ppb) on the morning of 28th September over the region of the Nord Stream gas leaks from (a) IASI; (b) TOMCAT using the decaying prior emissions; and (c) TOMCAT using the nocorr_1.0_plume posterior emissions based on that prior. Also shown is the difference between the model posterior and prior (d); the difference between IASI and the model prior (e); and the difference between IASI and the model posterior (f). Retrievals and model output are averaged onto 0.25° × 0.25° grid boxes, weighted inversely to the observations' uncertainties. IASI averaging kernels are applied to the TOMCAT output.

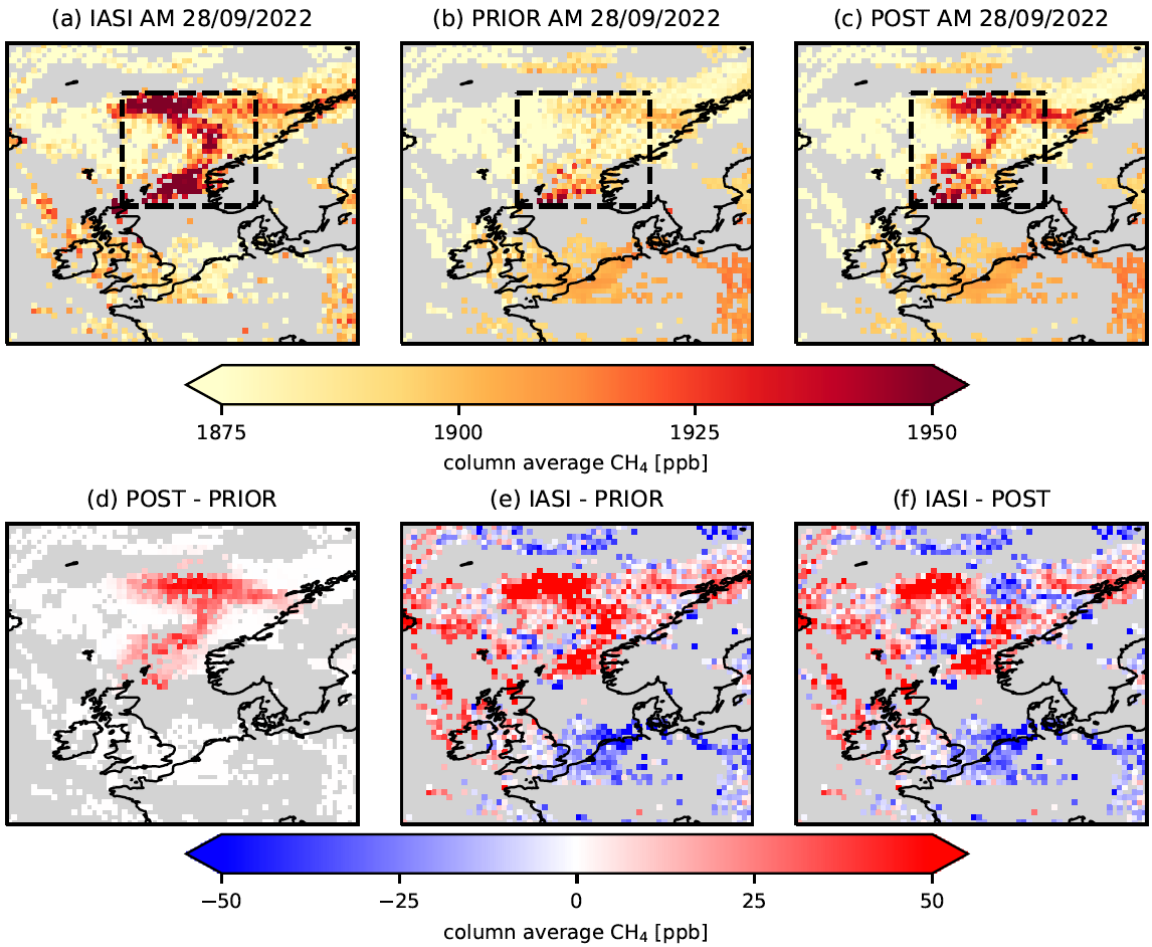

Figure S3: Column average CH_4 (ppb) on the morning of 28th September over the region of the Nord Stream gas leaks from (a) IASI; (b) TOMCAT using the constant prior emissions; and (c) TOMCAT using the nocorr_1.0_plume posterior emissions based on that prior for which the regional mean is optimised. Also shown is the difference between the model posterior and prior (d); the difference between IASI and the model prior (e); and the difference between IASI and the model posterior (f). Retrievals and model output are averaged onto 0.25° × 0.25° grid boxes, weighted inversely to the observations' uncertainties. IASI averaging kernels are applied to the TOMCAT output.

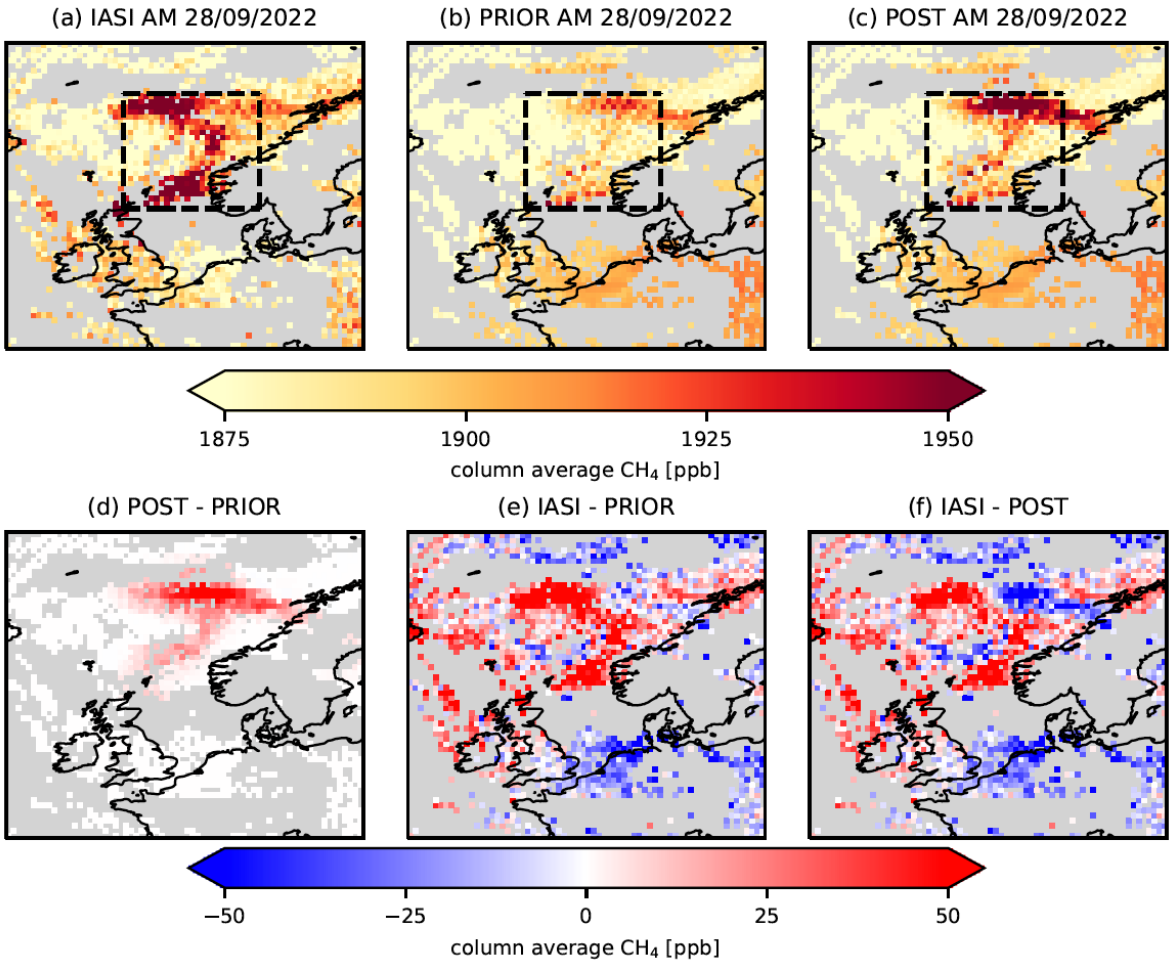

Figure S4: Column average CH_4 (ppb) on the morning of 28th September over the region of the Nord Stream gas leaks from (a) IASI; (b) TOMCAT using the decaying prior emissions; and (c) TOMCAT using the nocorr_1.0_plume posterior emissions based on that prior for which the regional mean is optimised. Also shown is the difference between the model posterior and prior (d); the difference between IASI and the model prior (e); and the difference between IASI and the model posterior (f). Retrievals and model output are averaged onto 0.25° × 0.25° grid boxes, weighted inversely to the observations' uncertainties. IASI averaging kernels are applied to the TOMCAT output.

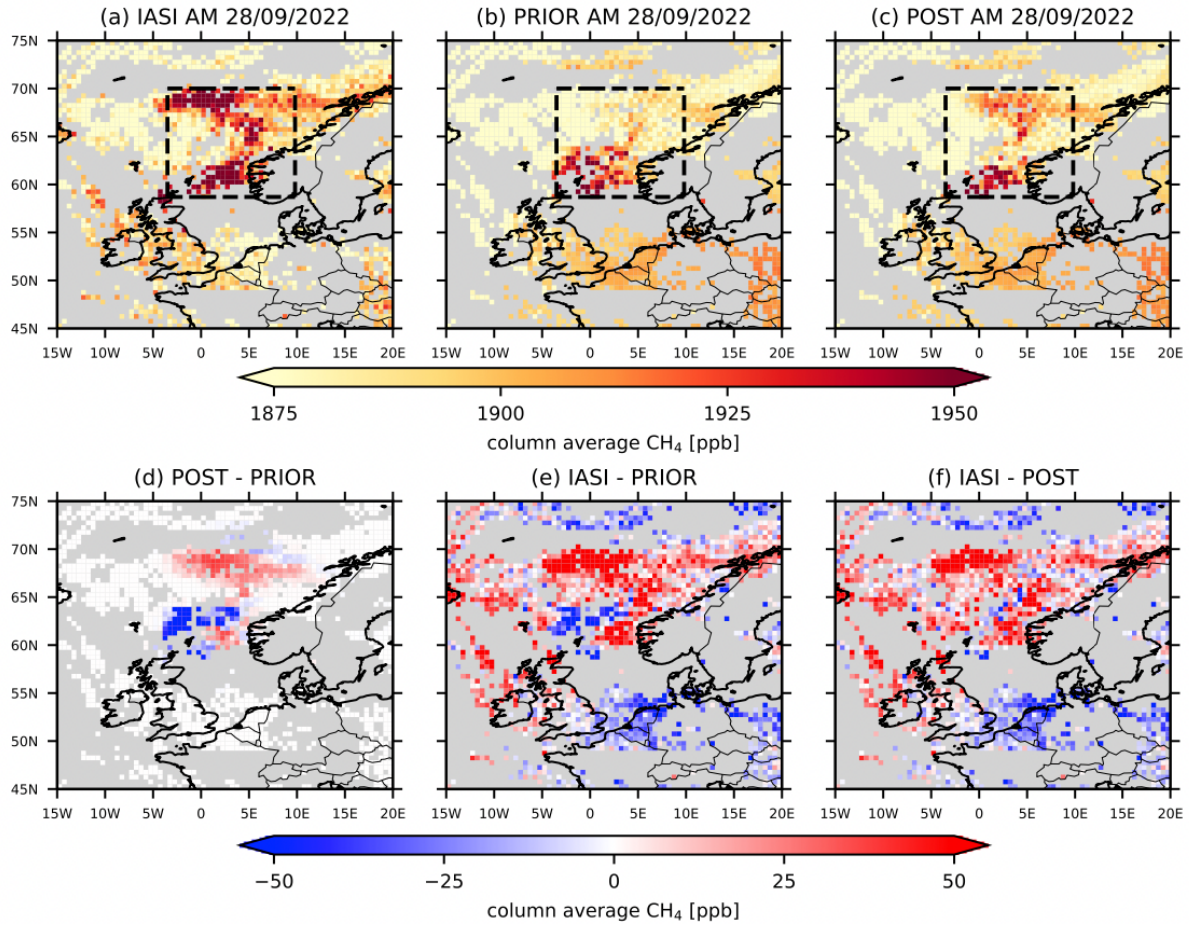

Figure S5: Column average CH_4 (ppb) on the morning of 28th September over the region of the Nord Stream gas leaks from (a) IASI; (b) TOMCAT using the modelled prior emissions; and (c) TOMCAT using the nocorr_1.0_plume posterior emissions based on that prior. Also shown is the difference between the model posterior and prior (d); the difference between IASI and the model prior (e); and the difference between IASI and the model posterior (f). Retrievals and model output are averaged onto 0.25° × 0.25° grid boxes, weighted inversely to the observations' uncertainties. IASI averaging kernels are applied to the TOMCAT output.

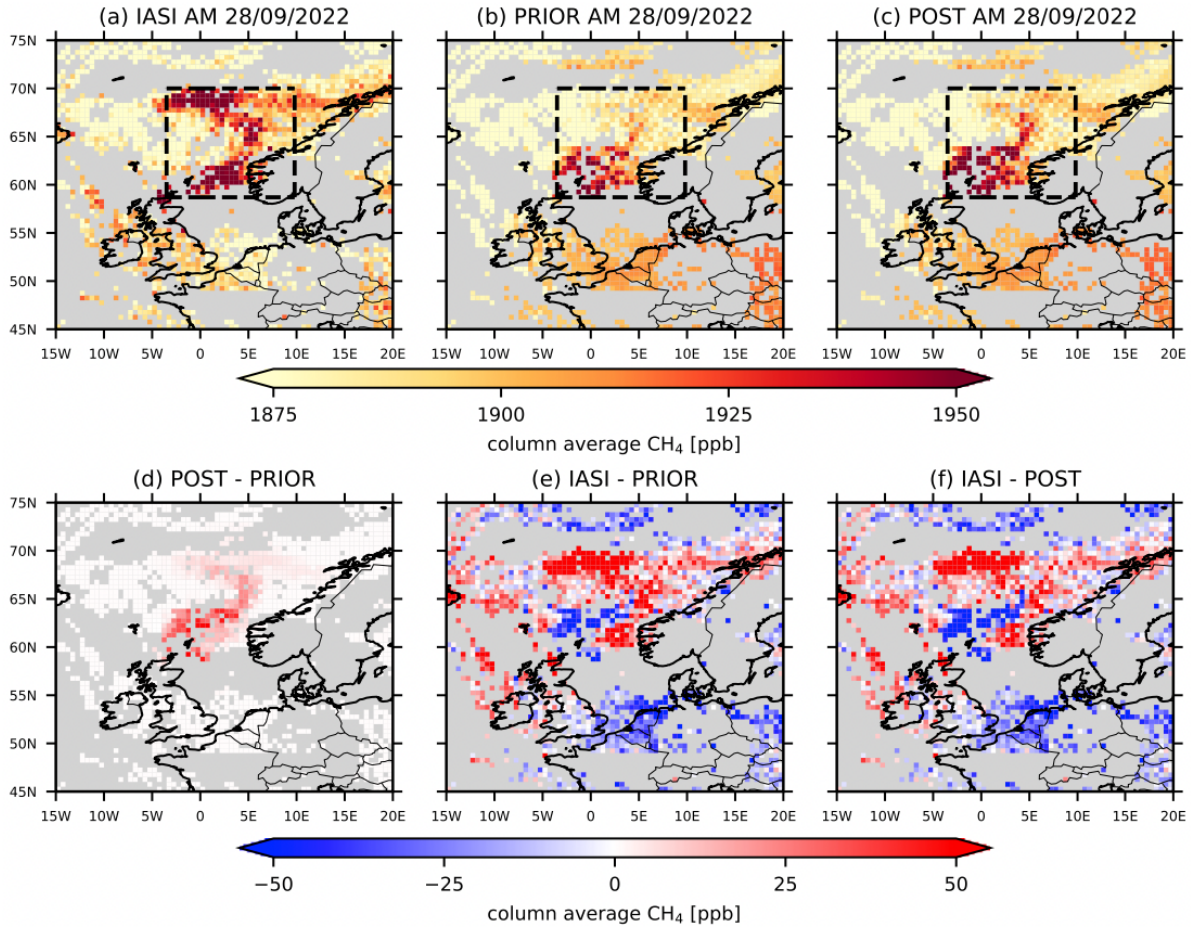

Figure S6: Column average CH_4 (ppb) on the morning of 28th September over the region of the Nord Stream gas leaks from (a) IASI; (b) TOMCAT using the modelled prior emissions; and (c) TOMCAT using the nocorr_1.0_plume posterior emissions based on that prior for which the regional mean is optimised. Also shown is the difference between the model posterior and prior (d); the difference between IASI and the model prior (e); and the difference between IASI and the model posterior (f). Retrievals and model output are averaged onto 0.25° × 0.25° grid boxes, weighted inversely to the observations' uncertainties. IASI averaging kernels are applied to the TOMCAT output.

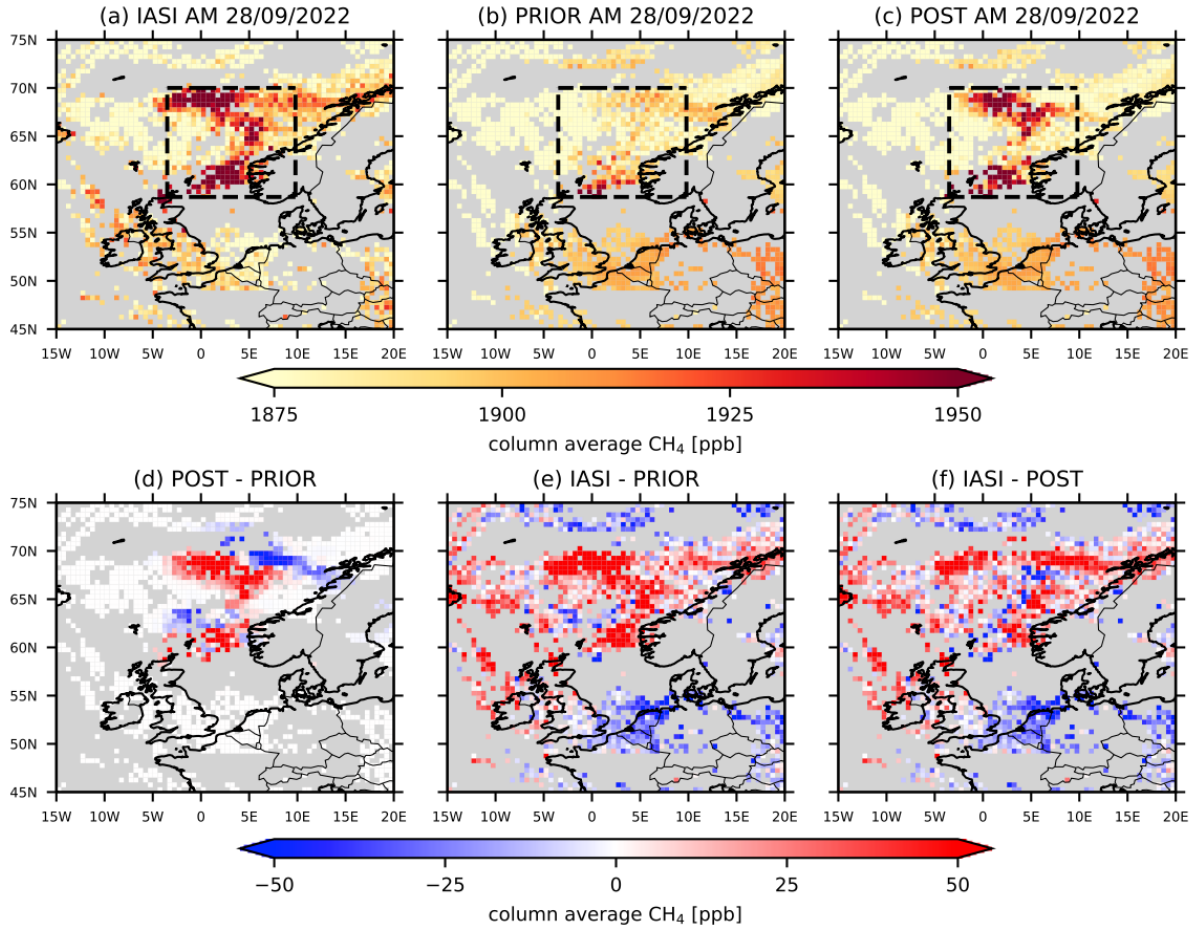

130 *Figure S7: Column average CH_4 (ppb) on the morning of 28th September over the region of the Nord Stream gas leaks from (a) IASI; (b) TOMCAT using the constant prior emissions; and (c) TOMCAT using the nocorr_1.0_plume posterior emissions based on that prior for which the 3° × 3° degree mean XCH_4 values are optimised. Also shown is the difference between the model posterior and prior (d); the difference between IASI and the model prior (e); and the difference between*
135 *IASI and the model posterior (f). Retrievals and model output are averaged onto 0.25° × 0.25° grid boxes, weighted inversely to the observations' uncertainties. IASI averaging kernels are applied to the TOMCAT output.*

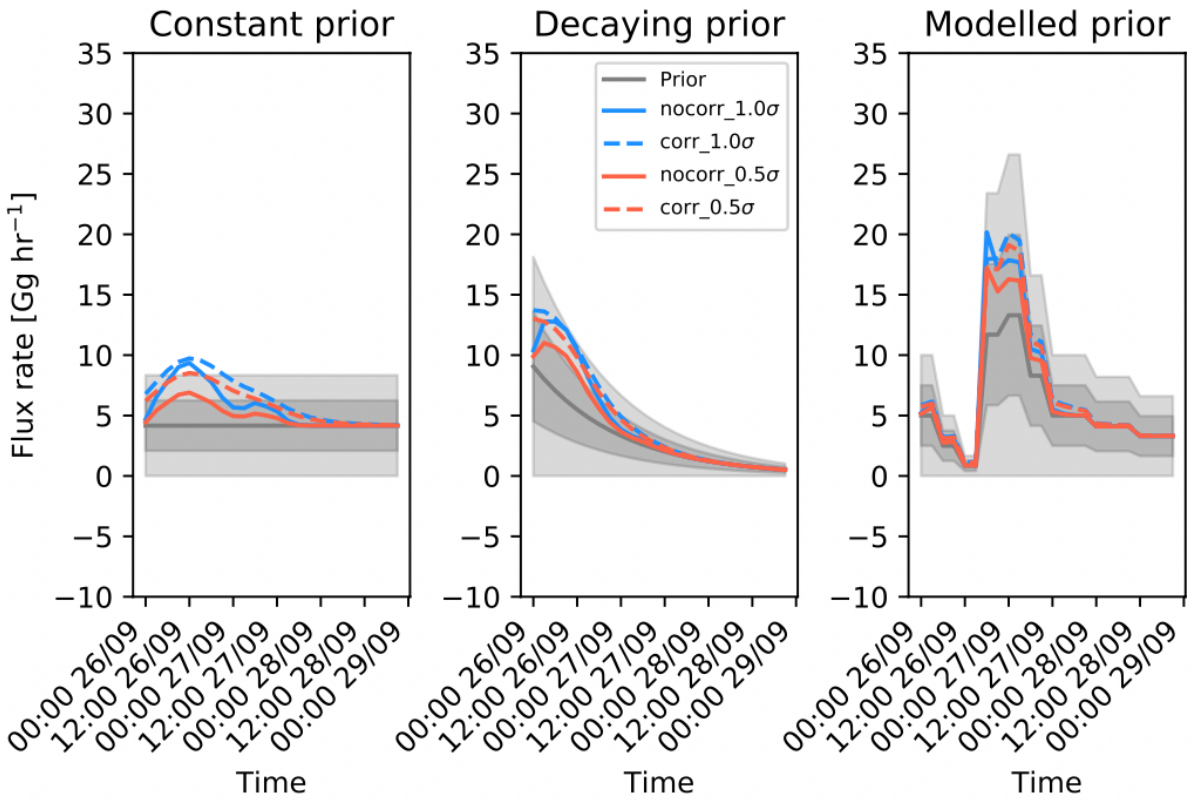

Figure S8: Prior and posterior flux rates (Gg hr^{-1}) over the first three days (September 26th - 28th) of the Nord Stream leaks based on IASI data from the morning of 28th September 2022. Posterior fluxes represent those when the regional mean in the region highlighted in ***Error! Reference source not found.*** *is optimised, rather than the individual retrievals. Prior flux rate is shown in grey, with dark grey shaded region showing the 50% prior uncertainty and the light grey shaded region showing the 100% prior uncertainty. Dashed lines show posterior inversions with prior temporal correlations imposed whilst solid lines show those without prior correlations. Blue lines show inversions with 100% prior uncertainty imposed, whilst red lines show those with 50% prior uncertainty.*

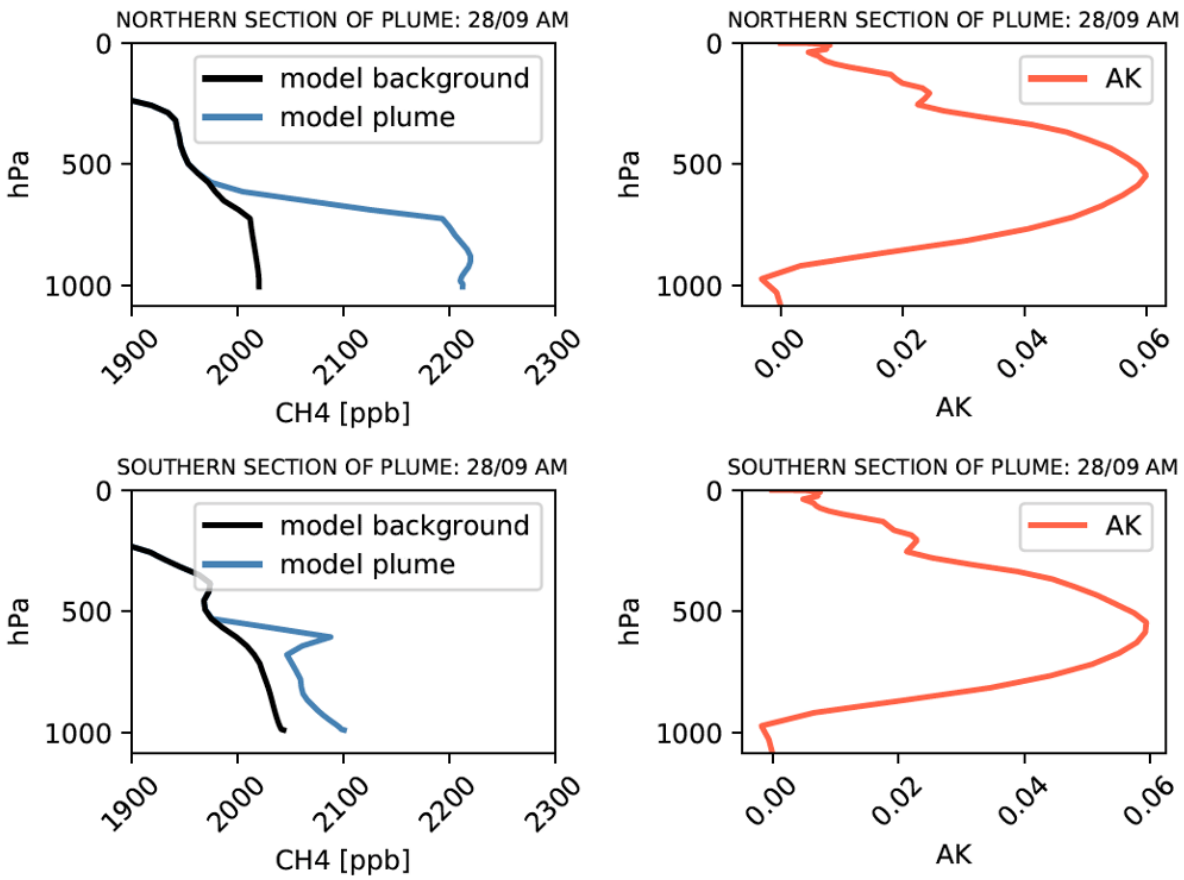

145

Figure S9: Simulated vertical profiles of CH_4 mixing ratios (ppb) in the northern (top left) and southern (bottom left) sections of the observed plume on the morning of 28th September 2022. Background CH_4 (black) and CH_4 from the Nord Stream leaks (blue) are highlighted separately. Also shown is the mean averaging kernel distribution for the IASI-retrieved column average CH_4 for the northern (top right) and southern (bottom right) sections of the plume.

150

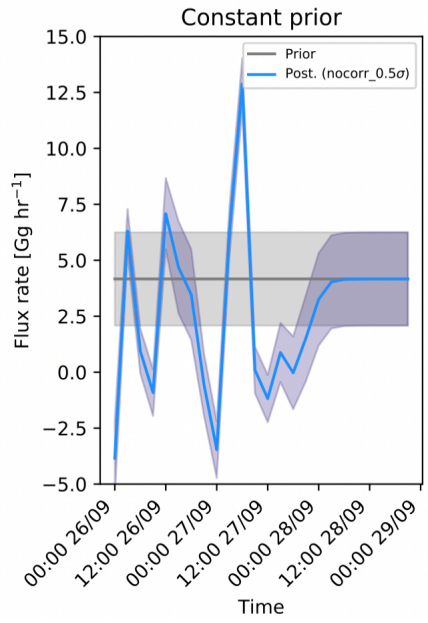

Figure S10: Prior and posterior flux rates (Gg hr^{-1}) over the first three days (September 26th - 28th) of the Nord Stream leaks based on ICOS data at NOR, BIR and UTO. HTM is excluded due to its proximity to the Nord Stream emission grid cell. Prior flux rate is shown in grey, with grey shaded region showing the 50% prior uncertainty. Blue line shows posterior fluxes.

Table S1: Total flux from Nord Stream leaks (Gg) over the first two days for all inversion scenarios. Uncertainties represent derived posterior uncertainty from the inversion. For the reported mean values in each column, we allocate the uncertainty as the largest uncertainty of the individual results instead of propagating the individual uncertainties, which often do not overlap.

	Constant prior (all data)	**Constant prior (plume only)**	**Constant prior (regional mean)**	**Decaying prior (all data)**	**Decaying prior (plume only)**	**Decaying prior (regional mean)**	**Modelled prior (all data)**	**Modelled prior (plume only)**	**Modelled prior (regional mean)**
nocorr_1.0	334 ± 23	291 ± 23	305 ± 37	270 ± 21	242 ± 23	292 ± 37	325 ± 26	287 ± 26	400 ± 54
corr_1.0	354 ± 25	304 ± 25	360 ± 57	291 ± 19	250 ± 20	324 ± 45	348 ± 28	304 ± 28	427 ± 72
nocorr_0.5	288 ± 14	254 ± 14	255 ± 22	247 ± 14	219 ± 14	258 ± 23	276 ± 16	246 ± 16	369 ± 35
corr_0.5	304 ± 16	263 ± 16	326 ± 36	264 ± 14	224 ± 14	306 ± 31	291 ± 18	257 ± 18	410 ± 48
Mean	320 ± 25	278 ± 25	312 ± 57	268 ± 21	234 ± 23	295 ± 45	310 ± 28	274 ± 28	402 ± 72

Table S2: Details of the different inversions carried out based on TOMCAT simulations of the Nord Stream methane plume. All combinations of the four criteria are included, giving 2 × 2 × 3 × 4 = 48 simulations in total.

	Options	**Number of options**
Temporal correlations	on/off	2
Prior flux uncertainty	50%/100%	2
Prior flux distribution	Constant/decaying/modelled	3
Observations assimilated	Plume/all/averaged/regional mean	4
	Total simulations =	48